A low loss and broadband complementary dual-output electro-optic modulator based on thin-film lithium niobate

Tingan Li (李廷安)[1], Chenglin Shang (尚成林) [1], Xuanhao Wang (王宣皓) [1], Weiqiang Lyu (吕伟强) [2], Zhiyao Zhang (张旨遥) [2], Cheng Zeng (曾成)[1]*, Yong Liu (刘永) [2] and Jinsong Xia (夏金松) [1]**

[1]Wuhan National Laboratory for Optoelectronics, Huazhong University of Science and Technology, Wuhan 430074, China

[2]State Key Laboratory of Electronic Thin Films and Integrated Devices, School of Optoelectronic Science and Engineering, University of Electronic Science and Technology of China, Chengdu 610054, China
*Corresponding author: zengchengwuli@hust.edu.cn; ** corresponding author: jsxia@hust.edu.cn

Received Month X, XXXX; accepted Month X, XXXX; posted online Month X, XXXX

Broadband, low-drive voltage electro-optic modulators are crucial optoelectronic components in the new-generation microwave photonic links and broadband optical interconnect network applications. In this paper, we fabricate a low-loss thin-film lithium niobate complementary dual-output electro-optic modulator chip with 3 dB electro-optic bandwidth of 59 GHz and half-wave voltage ($V\pi$) of 2.5 V. The insert-loss of the packaged modulator is 4.2 dB after coupling with polarization-maintaining fiber. The complementary dual-output modulator also shows a Common-Mode Rejection Ratio (CMRR) of 18 dB and signal enhancement of 6.2 dB when adapted in microwave photonic links, comparable to commercial bulk lithium niobate (LN) devices.
Keywords: Thin-film lithium niobate, electro-optic modulator, microwave photonic links.
DOI: 10.3788/COLXXXXXX.XXXXXX.

1. Introduction

As a fundamental element in microwave photonic systems, microwave photonic links (MPLs) could find diverse applications, including RF over fiber wireless communication[1], radio astronomy[2], and optical delay lines[3], etc. The MPLs technology have achieved huge developments, featuring high gain, low noise floor, and high linearity within constrained bandwidths. However, the widespread adoption of commercial MPLs faces challenges primarily due to noise over the useful bandwidth, including thermal noise, relative intensity noise (RIN), interference, and crosstalk[4-7], which originated from optical components like tunable lasers, Erbium Doped optical Fiber Amplifier (EDFA), modulators, etc. Among these components, the modulator plays a particularly crucial role. Its characteristics, including half-wave voltage (V_π), bandwidth, extinction ratio, and insertion loss, significantly impact the overall performance of MPLs[8,9]. Given that this noise introduces instability into the system, the development of low V_π and insertion loss, broad bandwidth modulators become necessary. Moreover, by utilizing dual-output modulators in conjunction with balanced photodetector (BPD)[10], it is possible to suppress the noise introduced by various components in the link, thereby enhancing the overall performance of MPLs.

As a newly proposed platform, Thin-Film Lithium Niobate (TFLN) exhibits a significant refractive index contrast between the LN waveguide and the cladding. It inherits nearly all the exceptional material characteristics of bulk LN but reducing the device footprint, becoming a promising candidate to replace bulk LN modulators in various applications. In recent years, low half wave voltage[11-14], broad-bandwidth[15-20], low insertion loss[21-25] thin-film lithium niobate modulators have been successfully developed[26]. However, there are still few reports on packaged dual-output Mach-Zehnder modulator (DO-MZM) based on a pure TFLN platform for the application in MPLs[27-30]. Moreover, integrating larger-sized spot size converters (SSCs) on the TFLN platform is necessary to achieve low-loss coupling with a polarization-maintaining fiber (YOFC PM1017E, 6.5μm mode field diameter) and reduce packaging loss.

In this work, a thin-film lithium niobate dual-output electro-optic modulator chip was fabricated, which consists of a Mach-zender interference (MZI) structure, a co-planar ground-signal-ground (GSG) electrodes, 6.5 μm spot-size converters, and a thermal-optical (TO) bias electrode. A symmetric 2 × 2 multi-mode interference (MMI) splitter is placed at the output of the chip to yield two outputs with intensities inversely proportional to each other. After packaging, the device exhibits a packaging loss of 4.2 dB with 3 dB electro-optic bandwidth of 48 GHz, half-wave voltage V_π of 2.5 V, and extinction ratio ≥ 25 dB. When utilizing a balanced photodetector (BPD) at the receiver end, 18 dB Common-Mode Rejection Ratio (CMRR) with 6.2 dB signal enhancement has been observed.

2. Device design

Fig. 1 (a) illustrates the designed dual-output modulator (DO-MZM) based on 500 nm thick X-cut TFLN, bonded on 4.7 μm thermally grown silicon dioxide with Si substrate (NanoLN). The device includes an electro-optic (EO)-MZI modulation region, a thermal-optical (TO) heater, 2x2 MMI, and spot size converters (SSC). In electro-optic (EO) modulation region, a 9-mm-long configuration with coplanar waveguide (CPW) travelling-wave electrode is utilized for the transmission of RF signals. A 200-μm-long, 7-μm-width Ti-heater is employed to adjust the bias points of the MZM structure through thermo-optical effect of LN, which is positioned above the LN waveguide and separated by a 1 μm thick SiO_2. For the input and output sections, 6.5 μm mode field diameter SSCs were utilized to maintain low coupling loss.

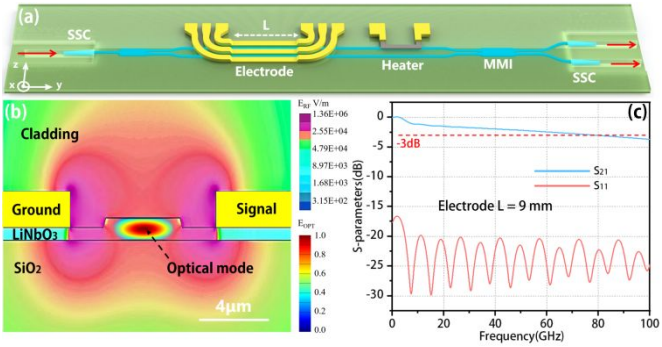

Fig. 1. (a) 3D schematic of the DOMZM; (b) Simulated optical field of the transverse electric (TE) mode and electric field distribution in the modulation region; (c) Simulated S-parameter of the designed CPW.

Fig. 1 (b) illustrates the cross-section diagram of the MZM modulation region. Where the optical signal is equally split into two paths and modulated by a co-planar ground-signal-ground (GSG) electrodes, the TE_0 mode and electric field distribution in the modulation region are shown in fig. 1 (b). The LN waveguide is designed as ridge waveguide with an etch depth of 260 nm and is broadened to 4 μm through an adiabatic taper waveguide. The gap between electrodes is set as 7.4 μm according to the trade-off between V_{π}, bandwidth, and the optical loss. Then the width of the signal electrode is set as 20 μm with an impedance close to 43 ohms, this value was chosen slightly lower than the characteristic impedance of the electrode (actual value of 47 ohm), which helps reduce the drop in the low-frequency S_{21} curve, to achieve a higher bandwidth. Fig. 1 (c) shows the simulation results of bandwidth, the 3 dB bandwidth is 67 GHz. A 1 × 2 and 2 × 2 multi-mode interference (MMI) couplers are utilized as splitter and combiner for the MZM configuration, respectively. The design of MMI is primarily based on the waveguide's self-imaging effect. To conserve space and reduce losses of the 2 × 2 MMI, a paired interference-type of MMI structure is employed[31]. In this configuration, the input optical field is distributed at $G = W_{MMI}/3$ around. Where G represents the gap between two waveguide and W_{MMI} represents the width of the MMI. Fig. 2 (a) illustrate the top view of the device, the optimized parameters are also marked on this figure. The power is divided equally at the two outputs. Optical field distribution of the device is shown in Fig. 2 (b), the splitting ratio at both ends is 49%.

To achieve efficient edge coupling between the TFLN waveguide and the polarization maintaining fiber, a spot size converter (SSC) with a mode field diameter (MFD) of 6.5 μm was designed. The structure of SSC is illustrated in Fig. 2 (c) and (d), which was achieved by modified our previous work of 3.2 μm SSC[32]. The 6.5 um SSC consists of three components, the lithium niobate taper, the SiON cladding waveguide, and the cladding silicon oxide. The refractive index of the SiON was tuned to be 1.56, between the lithium niobate and silicon oxide. By optimizing the size of the lithium niobate taper and the thickness of the SiON, TE_0 mode could propagate stably in SSC and highly matches with the fundamental mode field in 6.5 μm MFD polarization maintaining (PM) fiber. Furthermore, to achieve efficient transition of TE_0 modes between edge-coupler and lithium niobate taper and prevent excitation of higher-order modes, the lithium niobate taper should be located at the center of SiON cladding waveguide. Thus an additional etching of 3 μm depth is applied to the silicon oxide layer underneath the lithium niobate strip waveguide. A coupling loss of 0.04 dB per facet is obtained for TE mode in simulations after optimization as shown in Fig. 1 (e), which includes the mode conversion loss from cross-section C1 to C4. Fig.1 (f) shows the simulated optical field distribution in the SSC.

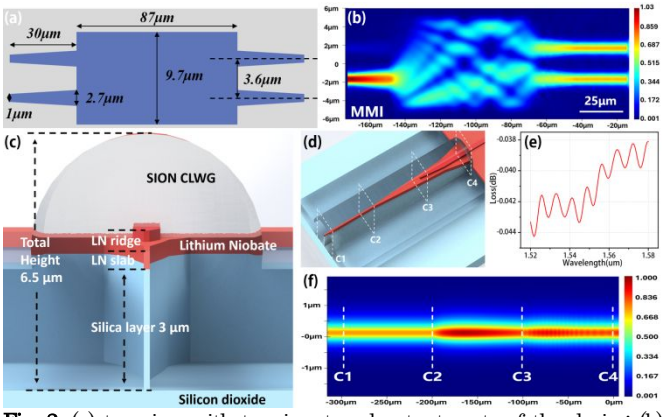

Fig. 2. (a) top view with two input and output ports of the device; (b) Simulated optical field distribution of the 2x2 MMI; (c) 3D schematic of the cross section of 6.5 μm mode field diameter SSC, SION CLWG: SION cladding waveguide; (d) 3D schematic of the SSC; (e) Simulated wavelength and loss curve of the SSC. (f) Simulated optical field of the transverse electric (TE) mode distribution in SSC. C1 to C4: the cross section of different part in SSC.

3. Fabrication and Measurement

The DO-MZM chip was fabricated on a commercial TFLN wafer (NANOLN). The chip has a compact footprint of 16 mm × 1.5 mm. The thicknesses of the LN and buried oxide layers are 500 nm and 4.7 μm, respectively. The fabrication process of the optical component is detailed in the following: electron beam lithography (EBL) was first used to define the ridge waveguide structures on the AR-P 6200 resist. Secondly, the patterns were transferred to the top LN layer with an etching depth of 260 nm by inductively coupled plasma (ICP) dry etching. Then, the strip waveguides for the edge coupler were defined on the LN layer with an etching depth of 3.24 μm using EBL and ICP dry etching, which include 0.24-μm LN taper and 3-μm buried oxide taper. At last, a SION layer with a thickness of 3.5 μm was deposited on the wafer as the cladding waveguide by plasma enhanced chemical vapor deposition (PECVD). More details can be found in Supplementary Material I.

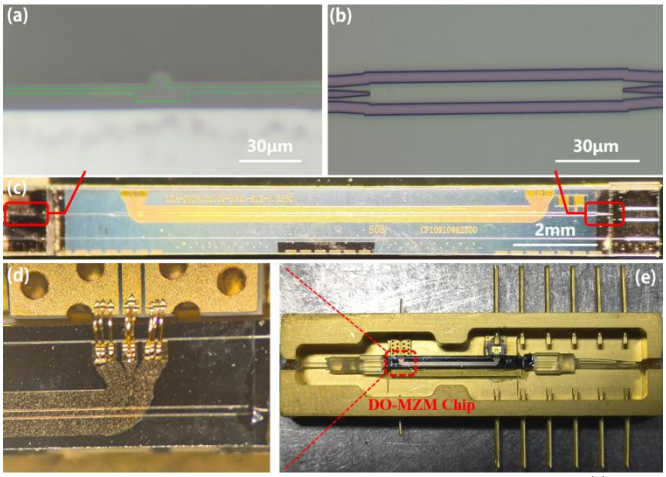

Fig. 3. The microscope image of details in dual-output MZM. (a) cross section of spot size converter (SSC); (b) Multimode Interference (MMI); (c) The overall photograph of the DOMZM; (d) Optical micrograph of the wire

bonded pad and ceramic transmission lines; (e) Photograph of the packaged DO-MZM device.

Microscope images of the fabricated sample are shown in Fig. 3 (a)-(c). The dual-output MZM chip was fabricated on a commercial TFLN wafer (NANOLN). Which has a compact footprint of 16 mm × 1.5mm. Following fabrication, optical and electrical packaging work was carried out on the device. In terms of optical packaging, the polarization-maintaining single-mode fiber (YOFC PM1017E) was chosen to achieve optimal mode-field matching, considering the MFD of the device's SSC at 1550nm is about 6.5 μm. The fiber arrays (FA) were aligned with the spot size converters and fixed by UV-curable glue. The LN chip within a custom-built metal tube shell can be seen in Fig. 3 (e). As for electrical packaging, the RF connection and DC bias connection parts are involved. The DC pad is wire bonded to the DC pins on the tube shell. Additionally, the input RF pad is wire bonded to the ceramic transmission line and connected to the 1.85-mm-long RF coaxial connectors. The ceramic transmission line, which consists of alumina ceramic with metal coplanar waveguide electrodes, has a thickness of 254 μm. Thus, the RF signal can be transmitted from the microwave source to the chip. To achieve impedance matching, a 43 ohms load resistor is attached at the end of the CPW travelling-wave electrode. Fig. 3 (d) illustrates that a group of gold wires are employed for electrical interconnection between the electrode and external load resistance.

After packaging, the optical characteristics were tested using a tunable laser (Santec TSL-550), a power meter (YOKOGAWA A02211) and a DC power source (GWINSTEK GPD-4303s). The DC transmission with TO phase shifters was initially measured. Fig. 4 (a) displays the TO transmission curve in relation to the applied voltage. The optical power output of the two ports is represented by the black and red lines, while the blue line represents the total power of both ports. Consequently, the fiber-to-fiber loss of the device amounts to -4.2 dB, accompanied by an extinction ratio (ER) of 25 dB. The results indicate that intensities of both ports are inversely proportional to each other. Notably, the length of the TO phase shifter is merely 200 μm with a resistance value of 350 Ω. The required voltages for achieving null bias points adjacent to each other are determined as 5 V and 8 V respectively, corresponding to P_{π} (power required for π-phase shift) of 55 mW. Additionally, the loss of 2 × 2 MMI is -0.14 dB, and the spectrum of the MMI can be observed in the insert of Fig. 4 (b), and further experimental details are available in our previous work[33]. The total loss comprises several factors: two spot size converter (SSC) ports contribute -3 dB (-1.5dB/facet), two MMIs account for -0.5 dB (with the 1 × 2 MMI at -0.35 dB and the 2 × 2 MMI at -0.14 dB), waveguide contributes to a loss of -0.3 dB (with propagation loss of -0.2 dB/cm). The remaining loss of -0.4dB is attributed to the modulation region which may cause by misalignment between different layers during EBL exposure, leading to an increase in metal absorption loss within the waveguide region. Fig. 4 (b) shows the half-wave voltage V_{π} measurements for DO-MZM with a 100 kHz triangular voltage sweep. The V_{π} value for the 9 mm long device is 2.5 V, corresponding to a $V_{\pi} \cdot L$ of 2.25 V·cm.

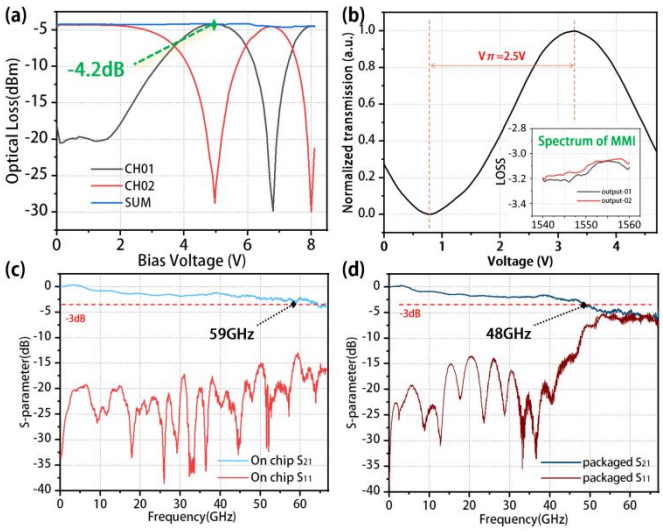

Fig. 4. (a) The voltage-loss curve of the device; (b) The voltage-power curve of the DOMZM under DC bias and the spectrum of 2*2 MMI; (c) The measured and calculated S-parameter curve; (d) The S-parameter curve of the device after packaging.

Then the EO responses of the fabricated device was characterized under the RF signal. As shown in Fig. 4 (c), the on chip 3-dB EO bandwidth (S_{21} parameter) of the DO-MZM is 59 GHz, and the input return losses (S_{11} parameter) is less than −15 dB at up to 58 GHz. After packaging, the EO bandwidth became 48 GHz as shown in Fig. 4 (d). The S_{11} is less than −10 dB at up to 47 GHz but increase beyond 47 GHz. The reasons are as fellows, Firstly, the RF input section is composed of RF connectors and RF pins, and both have specific working frequencies, which will cause the increase of reflections beyond 40 GHz. Secondly, there are discontinuities in the RF links between RF connectors and pins which will further degrade reflection performance. This issue can be solved by optimizing the connects between RF connectors and RF pins.

When paired with a Balanced Photodetector (BPD), the DO-MZM can restrain DC components, suppress common-mode noise, and enlarge the dynamic range of the MPLs. The responsivity of the two photodetectors in the BPD is η_1, η_2 and the noise is $n_1(t)$, $n_2(t)$. Hence, the response current of the photodetectors is obtained in Eq. (1) and (2):

$$i_1 = \eta_1 E_1 E_1^* = \eta_1\left[\frac{A^2+B^2}{2} + AB\cos\left(d\omega t + d\varphi - \frac{\pi}{2}\right)\right] + n_1(t), \quad (1)$$

$$i_2 = \eta_2 E_2 E_2^* = \eta_2\left[\frac{A^2+B^2}{2} + AB\cos\left(d\omega t + d\varphi + \frac{\pi}{2}\right)\right] + n_2(t), \quad (2)$$

Where E_1, E_2 represents the two output ports of the DO-MZM. $d\omega$ and $d\varphi$ stands for the angular frequency and phase difference between the two ports. A and B are amplitudes of E_1 and E_2, respectively, which are complementary to each other. According to Eq. (1) and Eq. (2), the total output current of the BPD i_{out} is given:

$$i_{out} = i_1 - i_2 = (\eta_1 - \eta_2)\frac{A^2+B^2}{2} + (\eta_1 + \eta_2)AB\cos\left(d\omega t + d\varphi - \frac{\pi}{2}\right) + n_1(t) - n_2(t), \quad (3)$$

Eq. (3) illustrates when dual-output modulator paired with BPD, according to $n_1(t) - n_2(t)$, common-mode noise could be suppressed to a lower level.

To test the DO-MZM's ability of the noise floor suppression in MPLs, we have constructed a balanced detection structure as shown in Fig. 5 (a). In this measurement, a continuous-wave light source was provided by a DFB laser with a center wavelength of 1550 nm (Santec TSL-510). The light passed through a variable optical attenuator (VOA) and an optical power amplifier (EDFA, Amonics AEDFA-IL-23-B-FA) before being directly coupled into the sample (DO-MZM). The bias point was then set at the linear operating point. Simultaneously, a microwave source (ROHDE&SCHWARZ SMB 100A) generated a 1 GHz signal at a power level of -25 dBm, which was applied to the DO-MZM. Subsequently, the two optical output signals of the device were gone through the Optical Time Delay Lines (OTDL) and variable optical attenuators (VOA) to ensure consistent delay ($d\varphi$) and power (A & B) levels. Finally, both signals were simultaneously input into the BPD.

To conduct a comparative analysis on the disparity in noise floor between the single output and dual output received by BPD, we individually connected the device's two ports, 01 and 02, to the BPD, respectively. The resulting output data is displayed in Fig. 5 (b) and 5 (c). The signal powers were measured at -49 dBm (Port 01) and -46 dBm (Port 02), with corresponding background noise levels of -65.04 dBm (range from -65.04 dBm to -68.63 dBm at 10 GHz) and -65.44 dBm (range from -65.44 dBm to -68.15 dBm at 10 GHz). Subsequently, both output ports were simultaneously connected to the BPD, as illustrated in Fig. 5 (d). The signal power increased to -41 dBm (both ports), while the signal's background noise decreased to -83.78 dBm (range from -83.78 dBm to -86.53 dBm at 10 GHz). Through this experiment, an 18 dB Common-Mode Rejection Ratio (CMRR) was measured. Additionally, by balancing the output power of ports 01 and 02, a signal enhancement of 6.2 dB was calculated. The CMRR and signal enhancement achieved in this study are comparable to those of commercial bulk LN devices, but with a more compact size and larger useful bandwidth.

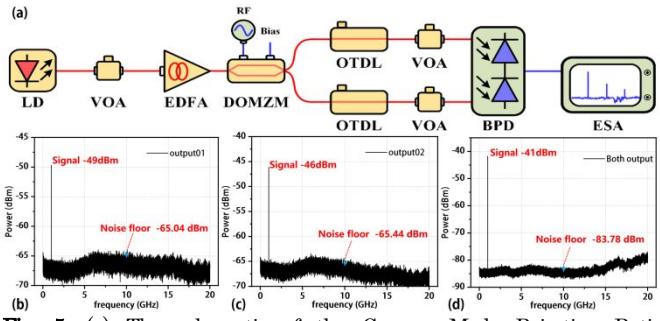

Fig. 5. (a) The schematic of the Common-Mode Rejection Ratio measurement set-up; (b) Power output of DOMZM when BPD connected to port 1; (c) Power output of DOMZM when BPD connected to port 2; (d) Power output of DOMZM when BPD connected to both 01 and 02 ports; LD: Laser Diode; VOA: Variable Optical Attenuator; EDFA: Erbium Doped Optical Fiber Amplifier; DOMZM: Dual-Output MZM; OTDL: Optical True Time Delay Line; BPD: Balanced Photodetector; ESA: Electronic Spectrum Analyzer.

4. Conclusion

In this work, a low loss, broadband TFLN electro-optic MZM with two opposite outputs was designed, fabricated, and characterized. The device shows an insertion loss of 4.2 dB, a half-wave voltage of 2.5 V, and a on chip 3-dB EO bandwidth of 59 GHz. A large bandwidth of 48GHz was achieved after package. When paired with a BPD receiver, an 18 dB CMRR and 6.2 dB signal enhancement is measured and calculated, respectively. TFLN has shown its advance in fabrication of ultra-low loss, low V_{π} and broad bandwidth modulators, and the footprint is more compact than those modulators based on bulk LN platforms. Our result shows the DO-MZM based on TFLN is promising for practical use in high performance MPLs.

5. Reference

[1] Anthony Ng'oma. "Radio-over-Fibre Technology for Broadband Wireless Communication Systems". Technische Universiteit Eindhoven, 2005.

[2] J. Mena, K. Bandura, and Q.Y. Tang et al. "A Radio-Frequency-over-Fiber link for large-array radio astronomy applications". 2013 JINST 8 T10003

[3] Sanghoon Chin, Luc Thévenaz, and Daniel Dolfi et al. "Broadband true time delay for microwave signal processing, using slow light based on stimulated Brillouin scattering in optical fibers". Optics Express. 11 October 2010. Vol. 18, No. 21. 11 October 2010. 22599-22613

[4] J. Davila-Rodriguez, F. N. Baynes, and F. Quinlan et al. "Compact, thermal-noise-limited reference cavity for ultra-low-noise microwave generation". Optics Letters. Vol. 42, No. 7. April 1 2017. 1277-1280

[5] Stéphanie Molin,* Ghaya Baili, and Jean-Pierre Huignard et al. "Experimental investigation of relative intensity noise in Brillouin fiber ring lasers for microwave photonics applications". Optics Letters. August 1, 2008. Vol. 33, No. 15. 1681-1683

[6] He Wen, Hongjun Zheng, and Guifang Li et al. "Few-mode fibre-optic microwave photonic links". Light: Science & Applications (2017) 6.

[7] Robert A. Minasian. "Photonic Signal Processing of Microwave Signals". IEEE Transactions On Microwave Theory and Techniques, Vol. 54, No. 2, February 2006

[8] Christian G. Bottenfield, Varghese A. Thomas, and Stephen E. Ralph et al. "Silicon Photonic Modulator Linearity and Optimization for Microwave Photonic Links". IEEE Journal of Selected Topics in Quantum Electronics. Volume 25. Issue 5, 2019.

[9] David Marpaung , Jianping Yao and José Capmany. "Integrated microwave photonics". Nature Photonics. VOL 13, February 2019. 80–90

[10] Yan Cui, Kun Xu*, and Yitang Dai, " Suppression of Second-Order Harmonic Distortion in ROF Links Utilizing Dual-Output MZM and Balanced Detection", 2012 IEEE International Topical Meeting on Microwave Photonics, September 2012.

[11] Dylan Renaud, Daniel Rimoli Assumpcao, Graham Joe et al, "Sub-1 Volt and high-bandwidth visible to near-infrared electro-optic modulators", Nature Communications, (2023) 14:1496

[12] Cheng Wang, Mian Zhang, Xi Chen et al, "Integrated lithium niobate electro-optic modulators operating at CMOS-compatible voltages", Nature, Vol. 562, 4 October 2018.

[13] A. N. R. Ahmed, S. Nelan, and D. W. Prather, "Subvolt electro-optical modulator on thin-film lithium niobate and silicon nitride hybrid platform", Opt. Lett., vol. 45, no. 5, Mar. 2020. 1112

[14] Y. Liu, H. Li, and W. Guo, et al. "Low V_{π} thin-film lithium niobate modulator fabricated with photolithography", Opt. Exp., vol. 29, no. 5, p. 6320, Mar. 2021.

[15] Brandon Buscaino, M. Zhang, Cheng Wang et al, "Broadband electro-optic frequency comb generation in a lithium niobate microring resonator", Nature, Vol. 568, 18 April 2019, 373-377.

[16] M. He, M. Xu, and X. Cai, et al. "High-performance hybrid silicon and lithium niobate Mach–Zehnder modulators for 100 Gbit/s and beyond", Nature Photon., vol. 13, no. 5, pp. 359-364, May 2019.

[17] A. J. Mercante, S. Shi, and D. W. Prather, "Thin film lithium niobate electro-optic modulator with terahertz operating bandwidth", Opt. Exp., vol. 26, no. 11, May 2018. 14810

[18] Forrest Valdez, Viphretuo Mere and Shayan Mookherjea et al. "110 GHz, 110 mW hybrid silicon - lithium niobate Mach - Zehnder modulator". Scientific Reports. 2022, 12: 18611

[19] Forrest Valdez, Viphretuo Mere, Xiaoxi Wang, and Shayan Mookherjea. "Integrated O- and C-band silicon-lithium niobate Mach-Zehnder modulators with 100 GHz bandwidth, low voltage, and low loss". Optics Express. Vol. 31, No. 4, 13 Feb 2023

[20] Viphretuo Mere, Forrest Valdez and Shayan Mookherjea. "Design and Fabrication of Hybrid Lithium Niobate Electro-Optic Modulators". IEEE International Conference on Emerging Electronics (ICEE), 2022.

[21] Mian Zhang, Cheng Wang, Marko Loncar et al, "Monolithic ultra-high-Q lithium niobate microring resonator", Optica, Vol. 4, No. 12, December 2017.

[22] Boris Desiatov, Amirhassan Shams-Ansari, Mian Zhang et al, "Ultra-low-loss integrated visible photonics using thin-film lithium niobate", Optica, Vol. 6, No. 3, March 2019, 380-384.

[23] Amirhassan Shams-Ansari, Guanhao Huang, Lingyan He et al, "Reduced material loss in thin-film lithium niobate waveguides", APL Photonics 7, 081301 (2022)
[24] Christian Reimer, Rebecca Cheng, M. Yu et al, "Integrated electro-optic isolator on thin-film lithium niobate", Nature Photonics, Vol. 17, August 2023, 666–671
[25] G. Chen, K. Chen, and L. Liu, "High performance thin-film lithium niobate modulator on a silicon substrate using periodic capacitively loaded traveling-wave electrode", APL Photon., vol. 7, no. 2, Feb. 2022.
[26] M. Zhang, C. Wang, and M. Lončar, et al. "Integrated lithium niobate electro-optic modulators: When performance meets scalability", Optica, vol. 8, no. 5, p. 652, May 2021.
[27] S. Nelan, A. Mercante, and D. W. Prather, "Compact thin film lithium niobate folded intensity modulator using a waveguide crossing", Opt. Exp., vol. 30, no. 6, p. 9193, Mar. 2022.
[28] S. J. Spector, M. W. Geis1, and G. R. Zhou2, et al. " CMOS-compatible dual-output silicon modulator for analog signal processing", Opt. Exp, vol. 16, no. 15, pp. 11027-11031, July. 2008.
[29] Yibeltal Chanie Manie , Run-Kai Shiu, and Peng-Chun Peng, et al. " Dual-Output Mach–Zehnder Modulator for Optical Access Networks", Fiber and Integrated Optics, Vol. 37, No. 5, 256–263, 2018.
[30] Sean P. Nelan, Andrew Mercante, and Shouyuan Shi, et al. " Ultra-High Extinction Dual-Output Thin-Film Lithium Niobate Intensity Modulator", IEEE Access, Volume 10, 100300-100311, 2022.
[31] Lung-Wei Chung, San-Liang Lee, and Yen-Juei Lin. "Principles and application of reduced beat length in MMI couplers". Optics Express. Vol. 14, No. 19, 18 September 2006.
[32] Changran Hu, An Pan and Jinsong Xia et al. "High-efficient coupler for thin-film lithium niobate waveguide devices". Optics Express. Vol. 29, No. 4, 15 February 2021.
[33] T Li, C Zeng, JS Xia, "QAM signal with electric field sensor based on thin-film lithium niobate", Chinese Opt Lett, Vol. 21, No. 12, December 2023.

6. Funding Sources

This work is supported by National Key Research and Development Program of China (2021YFB2800104)， and the National Natural Science Foundation of China under Grant No. 62175079，62205119. We thank the Center of Micro-Fabrication and Characterization (CMFC) of WNLO and the Center for Nanoscale Characterization & Devices (CNCD), WNLO of HUST for the facility support.

7. Supplementary Material I

Fabrication detail of the device.

The proposed dual-output modulator were fabricated using the process flow shown in Fig. 6 (I)-(VI), and each figure shows the modulation region and spot size converter (SSC) region, respectively. First, an TFLN wafer was patterned using an electron beam lithography system (EBL) on a 700 nm thick resist (AR-P 6200), a 260 nm thick LN layer was removed using Ar plasma by means of inductively coupled plasma reactive ion etching (ICP-RIE) technology with an etching rate of ~60 nm/min to form the ridge waveguide as shown in Fig. 6 (I). Then a 1000 nm thick silica was deposited on the waveguide by plasma enhanced chemical vapor deposition (PECVD) and was etched by ICP dry etching in the modulation region and SSC region, later the EBL and ICP step was repeated to form the 2nd LN taper and 3rd SiO2 layer, a 200 nm-thick thermal Ti layer was evaporated by electron beam evaporation (EBE) before the electrode pattern was defined by EBL. Subsequently, a 1200 nm thick Au was evaporated by EBE and lifted off to form the electrode as shown in Fig. 6 (III). Next, 3.5 um thickness of silicon oxynitride is grown on the whole chip by PECVD in which silane, ammonia as well as nitrous oxide is used, and the silicon oxynitride was etched to form the SION waveguide in the SSC region. Fig. 6 (V) illustrates a protective layer of 4000 nm thick silica was deposited onto the device surface by PECVD to prevent contamination-related losses from the sample. Finally, the pad of the electrode was etched by ICP-RIE technology as shown in Fig. 6 (VI).

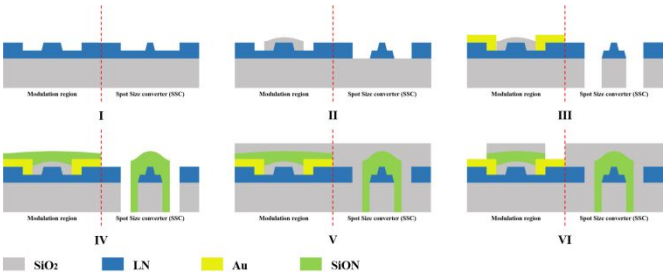

Fig. 6. Schematic illustration of the fabrication process of the CPW travelling-wave electrode and Spot size converter (SSC)